

# A study of the oxidation of FeCrAl alloy in pressurized water and high-temperature steam environment



Dong Jun Park\*, Hyun Gil Kim, Jeong Yong Park, Yang Il Jung, Jeong Hwan Park, Yang Hyun Koo

Korea Atomic Energy Research Institute, 989-111 Daedeok-daero, Yuseong-gu, Daejeon 305-353, Republic of Korea

## ARTICLE INFO

### Article history:

Received 2 December 2014

Accepted 21 February 2015

Available online 26 February 2015

### Keywords:

A. Alloy

B. TEM

B. XPS

C. Reactor conditions

C. High-temperature corrosion

C. Oxidation

## ABSTRACT

The oxidation behaviour of the FeCrAl alloy under normal operating conditions of a light water reactor is reported. In a comparative study, Zr-based and FeCrAl alloy samples were corroded in pressurized 360 °C water for up to 500 days or oxidized at 1200 °C for 3000 s in a steam environment. Compared to Zr-based alloys, the FeCrAl alloy showed extremely low weight change after both tests. The microstructure of the oxides formed on FeCrAl alloys was characterized by various analysing techniques. It was concluded that depending on the test conditions, mostly different oxide phases of  $\alpha$ -Fe<sub>2</sub>O<sub>3</sub> and  $\alpha$ -Al<sub>2</sub>O<sub>3</sub> were formed.

© 2015 Elsevier Ltd. All rights reserved.

## 1. Introduction

Zirconium-based alloys show fairly good resistance to corrosion under the operating conditions of a pressurized- or boiling-water reactor (PWR or BWR), as well as a very low absorption cross section of thermal neutrons with limited irradiation growth and creep. These attractive properties make them well suited for use as nuclear fuel cladding and structural components in conventional light water reactors (LWRs). However, the aggressive oxidation and significant heat production of Zr-based alloys in a high-temperature steam environment could significantly increase the risk of explosion caused by hydrogen gas [1,2], as seen in the Fukushima nuclear reactor accident. As a result, issues regarding the safety of nuclear plants during severe accidents and natural disasters were raised and solutions were discussed [3,4]. Although various approaches to enhance safety have been suggested, replacing current Zr-based alloys for fuel cladding with advanced materials exhibiting lower oxidation rates can be a basic solution [5,6]. Many advanced materials such as FeCrAl alloys;  $M_{n+1}AX_n$ , (phases, where  $n = 1-3$ , M is an early transition metal, A is an A-group (mostly IIIA and IVA, or groups 13 and 14) element and X is either carbon or nitrogen [7]; Mo [8]; and SiC [9,10] are being considered as possible candidates.

Among the proposed fuel cladding substitutes, Fe-based alloys are one of the most promising candidates owing to their excellent

formability, high strength, and oxidation resistance at high temperature. The excellent oxidation resistance of FeCrAl alloys at temperatures up to 1300 °C can facilitate their use in components operating at high temperature, e.g. in industrial furnace, heating elements, and catalytic converters [11]. For these high-temperature applications of FeCrAl alloys, their oxidation kinetics and mechanisms have been studied at a wide range of temperatures and in various environments [12–20]. Because nuclear-fuel claddings can be exposed to a high-temperature steam environment during certain nuclear reactor accidents caused by the loss of coolant, a clear understanding of the behaviour of FeCrAl alloys under those accident conditions is essential for their application in LWRs. However, although many researchers have reported on the effect of water vapour on the oxidation of FeCrAl alloys, their explanations of the oxidation mechanism remain a subject of controversy. While some researchers state that water vapour accelerates oxidation [21–23], others claim that it has little or no effect on the reaction [24–26]. Based on those previous studies, the oxidation of FeCrAl alloys at high temperature is expected to depend on the phase and microstructure of Al<sub>2</sub>O<sub>3</sub> scale formed on the surface. It has been reported that corrosion protection is provided by a slowly growing  $\alpha$ -Al<sub>2</sub>O<sub>3</sub> (corundum) phase [27,28]. In contrast, transient alumina such as  $\gamma$ -Al<sub>2</sub>O<sub>3</sub> (cubic),  $\delta$ -Al<sub>2</sub>O<sub>3</sub> (tetragonal), and  $\theta$ -Al<sub>2</sub>O<sub>3</sub> (monoclinic) results in rapid oxidation owing to the high defect concentration. Scale spallation caused by mechanical stress is another reason for the lack of protection [17].

In the pursuit of advanced nuclear-fuel cladding, the primary objective would be developing cladding materials with improved

\* Corresponding author. Tel.: +82 42 868 4849; fax: +82 42 862 0432.

E-mail address: [pdj@kaeri.re.kr](mailto:pdj@kaeri.re.kr) (D.J. Park).

properties and significantly improved behaviour during severe accidents, but their improved behaviour under normal operating conditions of a LWR is also an important criterion. In a PWR, light water used as the primary coolant is pressurized to approximately 15.5 MPa and heated to a temperature of about 315 °C. The coolant water remains in the liquid phase despite the high temperature because of the high pressure in the PWR reactor vessel. Although the corrosion of FeCrAl alloys under normal operating conditions of a PWR is one of the key factors that determine fuel performance and safety, it has not been studied in depth. To better understand how FeCrAl alloys behave during normal operation, it is crucial to perform the corrosion tests under conditions more pertinent to standard reactor operation for a prolonged period of time.

To summarize, to qualify as an advanced material for nuclear-fuel cladding, FeCrAl alloys should have greatly improved oxidation resistance during accidents and disasters while maintaining good corrosion resistance under normal operating conditions. The aim of the present study was to investigate the long-term corrosion of an FeCrAl alloy in a corrosive environment simulating the PWR coolant condition and its oxidation in a high-temperature steam environment. Various analytical techniques including scanning electron microscopy (SEM), transmission electron microscopy (TEM), X-ray diffractometry (XRD), and X-ray photoelectron spectroscopy (XPS) were used for the microstructural and quantitative analysis of the oxidized FeCrAl alloy samples. We found that depending on the exposure environment, completely different scales were formed on the FeCrAl alloy samples. A mechanism for the corrosion and oxidation of FeCrAl alloy in two different environments is also proposed.

## 2. Experimental

Kanthal APM alloy (Sandvik Heating Technology AB, Hallstahammar, Sweden), which is a ferritic FeCrAl alloy, was used in this study. This alloy consists of the main alloying elements and small amounts of additional alloying elements such as Si, Mn, and C. The nominal chemical composition (wt%) of the alloy is as follows: Cr, 22; Al, 5.8; Fe, balance. The surfaces of all specimens were ground with 2000-grit sandpaper and then ultrasonically cleaned in deionized water, acetone, and alcohol prior to the oxidation test.

To investigate the oxidation of the FeCrAl alloy in different environments in a nuclear reactor, two sets of experiments were performed under different conditions. In the first test, the alloy was corroded in pressurized 360 °C water representing the normal operating conditions of a nuclear reactor. For this long-term corrosion test, static autoclave has been used. Details of the test conditions are shown in Table 2. Ar gas bubbling was performed to reduce the oxygen content in the water prior to the autoclave test, but exact value of dissolved oxygen level was not measured. Hydrogen overpressure was not measured or controlled, either. To study the corrosion of the FeCrAl alloy over an extended period, the test was carried out for up to 500 days and the weight change of each sample was measured at set intervals using a microbalance with an accuracy of 0.01 mg. For comparison, two kinds of Zr-based alloys, referred to here as Z4 and ZL, were also corroded under the same test conditions. The chemical compositions of those alloys are given in Table 1. For all alloys used in this study, sets of 4 samples were introduced into the autoclave.

**Table 1**  
Chemical compositions (wt%) of Zr-based alloys.

Alloys	Nb	Sn	Fe	Cr	Zr
Z4	–	1.38	0.2	0.1	Bal.
ZL	1.0	1.0	0.1		Bal.

**Table 2**  
Corrosion test conditions.

	Temp. (°C)	Pressure (MPa)	Duration (days)	pH <sup>a</sup>
Water static autoclave	360	18.5	500	7.0– 7.5

<sup>a</sup> pH was measured at room temperature.

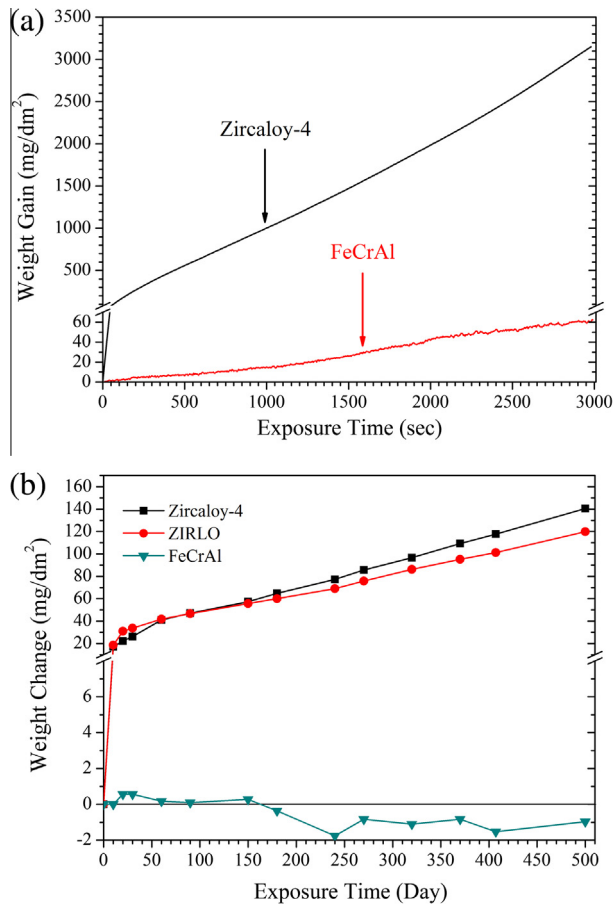
In the second test, alloy specimens were exposed to flowing water vapour at 1200 °C for 3000 s to simulate the conditions during a loss-of-coolant accident. A thermo-gravimetric analyser (TGA) was used to study the high-temperature oxidation of the FeCrAl alloy in the steam environment. Tests were conducted with heating rate of 50 °C/min to 1200 °C. To prevent oxidation during the temperature ramp, the test chamber of TGA was purged by Ar gas. The flowing steam was supplied into the chamber after reaching at 1200 °C. The furnace power was controlled by feedback from an R-type thermocouple placed near the sample. For this test, the weight change of the samples was measured in real time, and the degree of oxidation was evaluated in terms of weight gain per unit area.

The surface morphology of the oxides was investigated using field-emission SEM (FE-SEM; JSM6700F). The microstructural characterization of the oxide layer formed during the test was carried out using high-resolution TEM (HRTEM; JEM 3010) at 300 kV, and XRD (D/MAX-2500). For the HRTEM analysis, simulated images of the atomic arrangement were obtained using the program developed by the National Center for Electron Microscopy Simulation Software (NCEMSS) at the Lawrence Berkeley National Laboratory in Berkeley, California, USA. To determine the valences of the ions in the oxide layers, XPS (Sigma Probe) measurements were obtained. Peak fitting of the XPS spectra was performed using OriginPro7.5.

## 3. Results and discussion

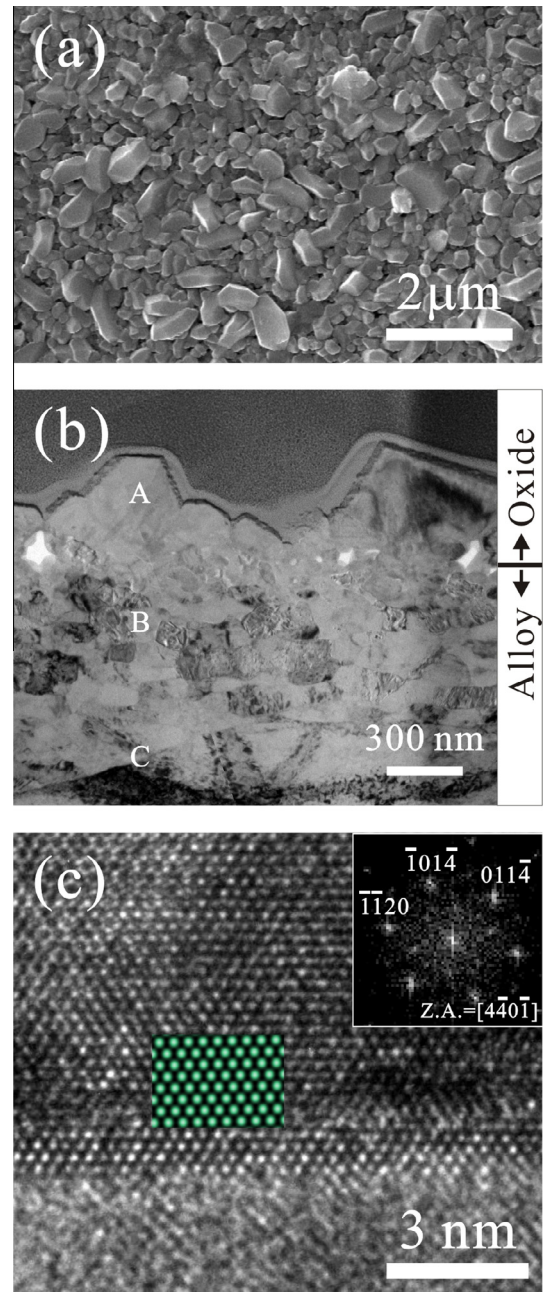
For the comparative study on the oxidation of FeCrAl and Zr alloys in a high-temperature steam environment, their weight gain during exposure to water vapour at 1200 °C was monitored; the results are shown in Fig. 1(a). As noted in Section 1, the Zr alloys (Z4, ZL) were rapidly oxidized. In contrast, the FeCrAl alloy exhibited an extremely low oxidation rate when compared to Zr alloys. After an exposure duration of 3000 s, the weight gain of the Zr-based alloy and the FeCrAl alloy was 3151.47 and 62.37 mg/d m<sup>2</sup>, respectively. To investigate the corrosion of both alloys in pressurized 360 °C water, static autoclave tests were carried out. Fig. 1(b) shows the averaged corrosion weight gain plotted as a function of autoclave exposure time for all alloys. During the first 50 days, the rate of corrosion of the Zr alloys was significantly high and then a slowdown in the weight increase was observed. We believe this change was primarily due to the thin oxide film (ZrO<sub>2</sub>) that formed initially on all Zr alloy surfaces and acted as a barrier to the migration of oxygen. In the case of the corroded FeCrAl alloy, a very small change in its weight was recorded after it had been exposed to steam for 500 days. Only a small increase in weight was observed during the first 30 days, and then the corroded samples exhibited weight loss. However, the maximum change in weight was just less than 2 mg/d m<sup>2</sup>.

Fig. 2(a) shows the surface morphology of the FeCrAl alloy sample that was corroded in pressurized 360 °C water for 240 days. Irregular islands ranging from about 10–930 nm in size were observed. It appears that continuous growth of nucleated oxide islands led to their coalescence. The cross-sectional microstructure near the interface between the oxide layer and the metal alloy



**Fig. 1.** Weight gain of the FeCrAl alloy after (a) oxidation in a steam environment at 1200 °C and (b) corrosion in pressurized 360 °C water.

matrix was characterized by TEM analysis; a bright-field TEM image is shown in Fig. 2(b). Oxide islands with different sizes were observed, and they showed certain planes on their surfaces. EDS analysis was carried out in regions marked A, B, and C in Fig. 2(b), and the results are shown in Table 3. The result from region A indicates that iron oxide was formed during the static autoclave test. The elemental compositions in regions B and C showed values that are similar to their nominal composition. Unlike general oxides formed on the metal, the corroded sample in our study showed pores located at the interface between the oxide and the metal matrix. It may be argued that those pores were formed during mechanical polishing and ion milling for the TEM sample preparation. However, this was impossible because all the TEM samples in this study were prepared by focused-ion-beam micromachining, which confirms that the observed pores were not related to mechanical damage during sample preparation. The mechanism of pore formation near the interface region of the corroded FeCrAl alloy may have been associated with the Kirkendall effect [29], where the outward diffusion rate of Fe in the oxide layer was much higher than the inward diffusion rate of oxygen. Similarly, Wang et al. studied the oxidation of iron nanoparticles and found that voids resided at the interface between the oxide shell and the iron core [30]. Quadackers et al. also reported that pore formation at the scale-metal interface could also occur if the scale growth largely proceeds by cation diffusion [31]. We believe that the phenomenon observed in our study can be explained by a similar mechanism. First, outward diffusion of iron cations through the oxide layer should have occurred during iron oxide growth. In this process, iron would have diffused from the



**Fig. 2.** (a) Plan-view SEM image of the surface morphology of the FeCrAl alloy that was corroded in 360 °C static water autoclave for 240 days. (b) Cross-sectional bright-field TEM image obtained from the vicinity of the interface between the oxide and the metal matrix. (c) Experimental HRTEM image of the interface region; the green rectangle represents the superposed simulated HRTEM image. The inset of (c) shows the fast-Fourier-transform (FFT) pattern.

**Table 3**

EDS point analysis results showing quantitative data (wt%) for the points labelled as A, B, and C in Fig. 2(b).

	Fe	Cr	Al	O
A	55.46	3.49	–	41.05
B	69.31	21.05	9.64	–
C	69.79	20.51	9.70	–

metal alloy to the interface region while aluminium and chromium would have diffused in the opposite direction. If the diffusivity of iron was much stronger than that of the other two elements,



vacancies would have been generated in the interface region. When the number of vacancies had increased sufficiently, their coalescence would have occurred, finally resulting in the formation of pores and local oxide spallation. It is concluded, therefore, that the weight loss of the FeCrAl alloy, shown in Fig. 1(b), can be explained by oxide spallation during corrosion in pressurized water.

To obtain more detailed microstructural information on the oxide layer, TEM analysis was carried out; the lattice structure and corresponding fast-Fourier transformed (FFT) pattern are shown in Fig. 2(c). Based on the distances and angles between spots in the FFT image, it was confirmed that iron(III) oxide ( $\text{Fe}_2\text{O}_3$ ) with a rhombohedral crystalline structure (corundum structure) was formed. An HRTEM image was obtained along the  $\langle 4\bar{4}0\bar{1} \rangle$  zone axis. The superimposed image in Fig. 2(c) is a simulated HRTEM image obtained using the NCEMSS program. Simulation was carried out using structural information of  $\alpha\text{-Fe}_2\text{O}_3$  (hematite) and the obtained atomic arrangement was viewed along the zone axis of  $\langle 4\bar{4}0\bar{1} \rangle$  at a defocus of 0 Å and a thickness of 20 Å. Note that the simulated HRTEM image is in agreement with the atomic arrangement of the experimental HRTEM image.

Fig. 3 represents the experimental and calculated XPS spectra of the oxide layer of the corroded sample in the binding energy range of 707–729 eV, which includes the Fe  $2p_{3/2}$  and Fe  $2p_{1/2}$  peaks. Spectral decompositions of the Fe 2p peaks were conducted to quantitatively evaluate the oxidation process. The Fe 2p lines were fitted to two oxidation states at 709.7 (Fe(II)) and 711.1 eV (Fe(III)) and shake-up satellite peaks at 714 and 718 eV. These values are very good matches to values reported in the literature [32–35]. The broad peak at 710.4 eV due to dual iron oxidation states indicates the existence of  $\text{Fe}_3\text{O}_4$  in the oxide layer. The satellite peaks at about 714 and 718 eV, on the other hand, are characteristic peaks of  $\text{Fe}^{2+}$  in FeO and  $\text{Fe}^{3+}$  in  $\alpha\text{-Fe}_2\text{O}_3$  (or  $\gamma\text{-Fe}_2\text{O}_3$ ), respectively. In contrast,  $\text{Fe}_3\text{O}_4$  usually shows no satellite peak in its 2p spectrum. Thus, the XPS spectra may confirm the presence of FeO,  $\text{Fe}_3\text{O}_4$ , and  $\alpha\text{-Fe}_2\text{O}_3$  (or  $\gamma\text{-Fe}_2\text{O}_3$ ) phases in the oxide layer on the surface of the corroded FeCrAl alloy. However, because the XPS Fe 2p spectra of  $\alpha\text{-Fe}_2\text{O}_3$  and  $\gamma\text{-Fe}_2\text{O}_3$  are almost identical to each other despite their large differences in crystal structures [36,37], it was not easy to distinguish  $\alpha\text{-Fe}_2\text{O}_3$  and  $\gamma\text{-Fe}_2\text{O}_3$  in our XPS spectra. Therefore, another characterization technique, X-ray diffraction, was used to differentiate the structures of the iron oxides; these results will be discussed later.

The formation of an oxide layer on the surface of the FeCrAl alloy sample that was oxidized at 1200 °C for 3000 s was observed

using TEM, and its cross-sectional bright-field TEM image is shown in Fig. 4(a). The average oxide thickness was approximately 480 nm and the thickness did not change significantly with position. The surface of the oxide particles was uneven and mixed columnar and equiaxed grains were observed in the oxide layer. The very low oxidation rate (shown in Fig. 1(a)) and the thin oxide layer formed after a relatively long exposure time indicate that water vapour had little effect on the high-temperature oxidation of the FeCrAl alloy. EDS line analysis was carried out to investigate the elemental distribution inside the oxide layer and the neighbouring metal alloy. EDS measurements were obtained along the line shown in Fig. 4(a), and the variations in the population of each element are shown in Fig. 4(b). Most of the oxide layer consisted mainly of Al and O and their steady intensity indicates a homogeneous chemical composition over the entire cross section. It is well known that FeCrAl alloys tend to form protective  $\alpha\text{-alumina}$  (corundum) layers on their surface at high temperature [21,38,39], resulting in the significantly reduced oxidation rate of FeCrAl alloys in high-temperature environments. However, even though it is certain that the oxide layer in our FeCrAl alloy sample consisted of Al and O, the EDS study was not sufficient to confirm that the grown oxide was  $\alpha\text{-Al}_2\text{O}_3$ . Thus, further microstructural characterization on the oxide layer was carried out, as shown by the results in Fig. 5. Interestingly, we discovered a continuous band of precipitates with spherical shapes, parallel to the interface between the oxide and the metal alloy. The EDS data showed that this band of precipitates (shown in Figs. 4(a) and 5(a)) was a Cr-enriched region (indicated by the arrow in Fig. 4(b)). This Cr band has

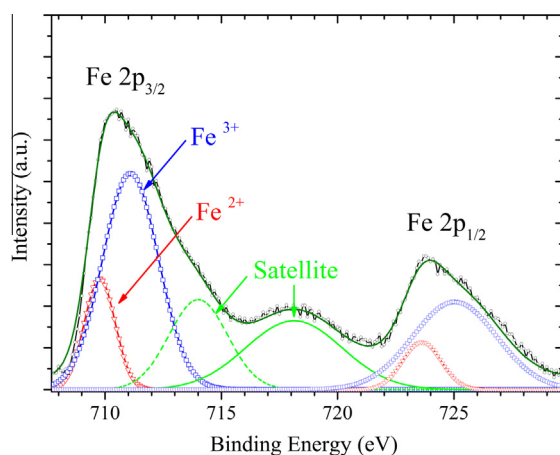


Fig. 3. Multi-peak fitted Fe 2p spectra taken from the surface of the FeCrAl alloy that was corroded in 360 °C water over a 240-day period.

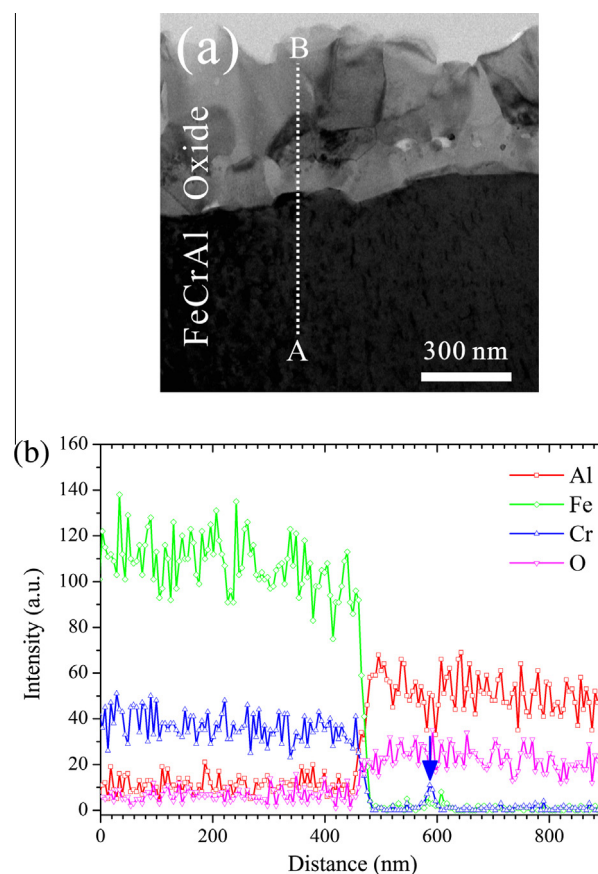
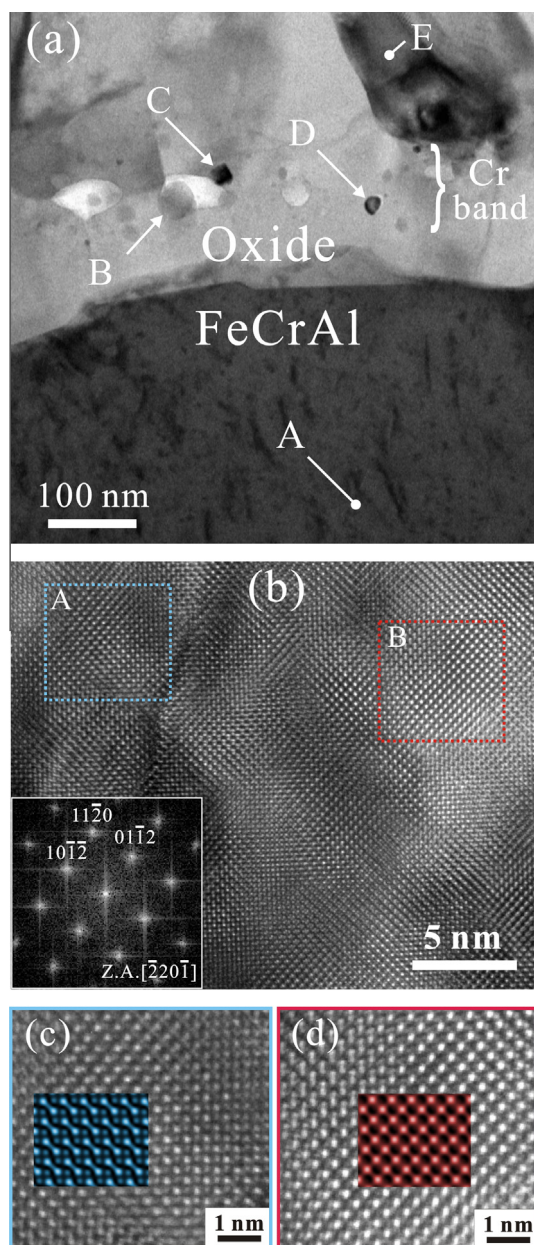


Fig. 4. (a) Cross-sectional TEM image of the oxidized FeCrAl alloy sample. (b) EDS line analysis from the metal to the oxide layer; the position of the EDS analysis is marked by the dotted line in (a).



**Fig. 5.** (a) BF-TEM image obtained from the region near the interface between the oxide layer and the FeCrAl alloy matrix. (b) HRTEM image of oxide layer with its FFT image in the inset. Enlarged views of the square regions indicated by A and B in (b) and their simulated lattice images are shown in (c) and (d), respectively.

been reported in earlier studies of oxidized FeCrAl materials at high temperature [12,17,40]; the Cr-enriched zone observed at the interface of duplex alumina scale and the Cr-rich zone originated in the native oxide present on the alloy surface before exposure. In these works, it was speculated that the presence of Fe and Cr in the oxide layer indicated an inward growth mechanism: even though oxygen preferentially reacted with Al and iron and chromium was rejected far from the growing oxide layer, their back diffusion needed time. As a result, we conclude that the top alumina layer in our sample was formed by outward diffusion of aluminium ions, while the bottom layer was formed by inward diffusion of oxygen.

To analyse the microstructure in more detail, enlarged cross-sectional TEM images of the interface between the oxide layer and the FeCrAl metal alloy were obtained, as shown in Fig. 5(a).

EDS point analysis was carried out for the spherical precipitates shown in Fig. 5(a), and the results are shown in Table 4. In addition to Cr, Fe was also present; however, a much higher amount of Cr was detected compared to Fe. Both Cr and Fe concentrations in the precipitates varied depending on their location, showing that they were not homogeneously distributed inside the precipitates.

It is known that the top and bottom layers of an FeCrAl alloy show different microstructures of stable  $\alpha$ -Al<sub>2</sub>O<sub>3</sub> and metastable  $\gamma$ -Al<sub>2</sub>O<sub>3</sub>, respectively. In this study, however, most of the oxide was  $\alpha$ -Al<sub>2</sub>O<sub>3</sub> regardless of its position. The HRTEM image in Fig. 5(b) shows the representative microstructure of the oxide layer. The distances and angles between spots in the FFT image obtained from the HRTEM image indicates that  $\alpha$ -Al<sub>2</sub>O<sub>3</sub> with a corundum structure was formed. The zone axis of the HRTEM image was  $\langle 220\bar{1} \rangle$ . Although experimental HRTEM images showed different lattice images based on their positions (indicated as blue and red squares), their diffraction patterns (FFT image) were the same. To verify this, simulated HRTEM images were obtained using the NCEMSS program at various values of defocus and sample thickness, as shown by the superimposed images in Fig. 5(c) and (d). The simulation was carried out using structural information of  $\alpha$ -Al<sub>2</sub>O<sub>3</sub> and the atomic arrangement viewed along the  $\langle 220\bar{1} \rangle$  zone axis. To obtain the superimposed image in Fig. 5(c), simulation was carried out at a defocus of  $-100$  Å and a thickness of  $150$  Å. On the other hand, the superimposed image in Fig. 5(d) was obtained by simulation at a defocus of  $-175$  Å and a thickness of  $75$  Å. Note that the simulated HRTEM images are in agreement with the atomic arrangement of the experimental HRTEM images. It appears, therefore, that the different atomic arrangements observed in the HRTEM images may have been caused by different thicknesses or some bending at different locations on the TEM specimen.

Fig. 6 shows a comparison of the X-ray diffraction patterns of the specimens that were corroded in  $360$  °C pressurized water or oxidized at  $1200$  °C for  $3000$  s.  $\gamma$ -Fe<sub>2</sub>O<sub>3</sub> and Fe<sub>3</sub>O<sub>4</sub> showed almost the same XRD patterns owing to their similar structures. However, the XRD pattern of  $\alpha$ -Fe<sub>2</sub>O<sub>3</sub> can be easily distinguished from that of  $\gamma$ -Fe<sub>2</sub>O<sub>3</sub> or Fe<sub>3</sub>O<sub>4</sub> [41–43]. Thus, all the diffraction peaks of the corroded FeCrAl alloy, shown in Fig. 6(a), can be readily indexed to the pure rhombohedral phase of  $\alpha$ -Fe<sub>2</sub>O<sub>3</sub> (JCPDS card No. 33-0664). Although XPS results (Fig. 3) indicated the presence of several oxide phases in the oxide layer, the analysis was carried out at depths of only  $8$ – $10$  nm from the surface. It can be concluded, therefore, that most of the oxidized state in the corroded FeCrAl alloy sample was  $\alpha$ -Fe<sub>2</sub>O<sub>3</sub> and the relative concentration of Fe<sub>3</sub>O<sub>4</sub> was extremely small. When the FeCrAl alloy was oxidized in steam at  $1200$  °C, only the XRD reflections attributed to  $\alpha$ -Al<sub>2</sub>O<sub>3</sub> and the metal substrate were observed (JCPDS card No. 46-1212). This result is consistent with the results obtained from EDS analysis (Fig. 4(a)) and TEM observations (Fig. 5). Consequently, it can be concluded that the FeCrAl alloy showed different phases of oxide according to the oxidizing temperature and environment. As shown in Fig. 6, one sample showed a single phase of  $\alpha$ -Fe<sub>2</sub>O<sub>3</sub> while the other showed a single phase of  $\alpha$ -Al<sub>2</sub>O<sub>3</sub>.

**Table 4**

EDS point analysis results showing quantitative data (wt%) for the points labelled as A, B, C, D, and E in Fig. 5(a).

	Fe	Cr	Al	O
A	69.89	22.15	7.96	–
B	16.39	32.79	22.83	27.98
C	7.51	11.35	37.02	44.13
D	2.81	16.84	35.61	44.74
E	2.93	2.3	42.31	52.46

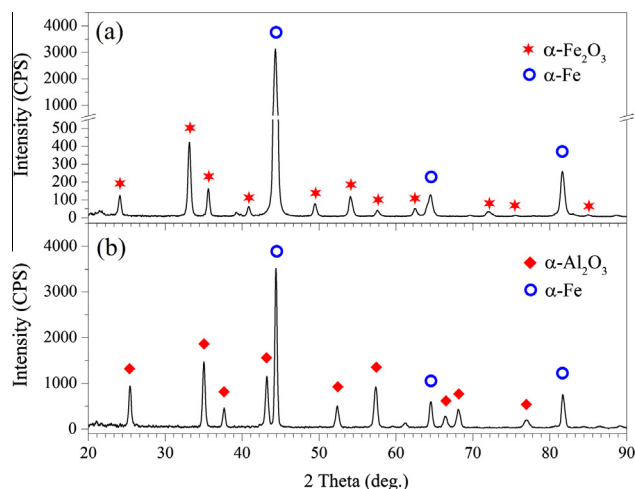


Fig. 6. XRD patterns of FeCrAl alloys that were (a) corroded in 360 °C pressurized water and (b) oxidized in a 1200 °C steam environment.

#### 4. Conclusion

To investigate the oxidation of the FeCrAl alloy in normal operating and accident condition of LWR, FeCrAl alloy samples were corroded at 360 °C for up to 500 days or oxidized at 1200 °C for 3000 s. After both tests, the oxidation of the FeCrAl alloy and the microstructure of the oxide layer were examined by various analytical techniques. Based on the results, the following conclusions were drawn:

1. The FeCrAl alloy showed superior corrosion and oxidation resistance compared to Zr-based alloys used as current nuclear-fuel cladding. However, depending on the test conditions, there were significant differences in the oxidation mechanisms of the FeCrAl alloy samples and the phases of the oxide layer.
2. The FeCrAl alloy that was corroded at 360 °C in pressurized water exhibited weight loss. Although various iron oxide phases such as FeO, Fe<sub>3</sub>O<sub>4</sub>, and α-Fe<sub>2</sub>O<sub>3</sub> were present near the outer oxide surface, the primary phase was α-Fe<sub>2</sub>O<sub>3</sub>.
3. There were pores at the interface between the oxide layer and the metal matrix of the corroded FeCrAl alloy. They resulted from the coalescence of voids caused by the much stronger out diffusion of iron compared to the inward oxygen diffusion. It is assumed that local oxide spallation was caused by these pores, which may have resulted in the weight loss during the corrosion test.
4. In contrast, the FeCrAl alloy showed weight gain after oxidation in the 1200 °C steam environment. In this test, an oxide layer of α-Al<sub>2</sub>O<sub>3</sub> corundum was mainly formed on the surface and a continuous band of precipitates, parallel to interface between oxide and metal alloy, was observed. In addition to Cr, iron was also enriched in the precipitates. This precipitation band indicates the original alloy surface before the test. The test showed that water vapour had little effect on the oxidation rate of the FeCrAl alloy.

#### Acknowledgement

This work was supported by the National Research Foundation of Korea (NRF) grant funded by the Korea government (MSIP) (No. 2012M2A8A5000702).

#### References

- [1] P. Hofmann, Current knowledge on core degradation phenomena, a review, *J. Nucl. Mater.* 270 (1999) 194–211.
- [2] M. Moalem, D.R. Olander, Oxidation of zircaloy by steam, *J. Nucl. Mater.* 182 (1991) 170–194.
- [3] K. Barrett, S. Bragg-Sittton, D. Galicki, Nuclear Fuel Cladding System Development Trade-off Study, Light Water Reactor Sustainability Program, U.S. Department of Energy, Idaho Falls, ID: Idaho National Laboratory, 2012, External Report. INL/EXT-12-27090.
- [4] S. Bragg-Sittton, Advanced LWR Nuclear Fuel Cladding System Development Technical Program Plan, Light Water Reactor Sustainability Program, U.S. Department of Energy, Idaho Falls, ID: Idaho National Laboratory, 2012, External Report. INL/MIS-12-25696.
- [5] K.A. Terrani, S.J. Zinkle, L.L. Snead, Advanced oxidation-resistant iron-based alloys for LWR fuel cladding, *J. Nucl. Mater.* 448 (2013) 420–435.
- [6] L.J. Ott, K.R. Robb, D. Wang, Preliminary assessment of ATF on LWR during normal operation and under DB and BDB accident conditions, *J. Nucl. Mater.* 448 (2013) 520–533.
- [7] J.Y. Park, I.H. Kim, Y.I. Jung, H.G. Kim, D.J. Park, B.K. Choi, High temperature steam oxidation of Al 3Ti-based alloys for the oxidation-resistant surface layer on Zr fuel claddings, *J. Nucl. Mater.* 437 (2013) 75–80.
- [8] B. Cheng, Fuel Behavior in Severe Accidents and Potential Accident Tolerance Fuel Designs, OECD-NEA Meeting, Paris, France, December 11, 2012.
- [9] H. Feinroth, Mechanical Strength of CTP Triplex SiC Fuel Clad Tubes After Irradiation in MIT Research Reactor, 33rd International Conference on Advanced Ceramics & Composites, Florida, January 20, 2009.
- [10] D.J. Park, Y.I. Jung, H.G. Kim, J.Y. Park, Y.H. Koo, Oxidation behavior of silicon carbide at 1200 °C in both air and water-vapor-rich environments, and Fe-based alloys, *Corros. Sci.* 88 (2014) 416–422.
- [11] C. Badini, F. Laurella, Oxidation of FeCrAl alloy: influence of temperature and atmosphere on scale growth rate and mechanism, *Surf. Coat. Technol.* 135 (2001) 291–298.
- [12] J. Engkvist, S. Canovic, K. Hellström, A. Järnäs, J.E. Svensson, L.G. Johansson, M. Olsson, M. Halvarsson, Alumina scale formation on a powder metallurgical FeCrAl alloy (Kanthal APMT) at 900–1100 °C in Dry O<sub>2</sub> and in O<sub>2</sub> + H<sub>2</sub>O, *Oxid. Met.* 73 (2010) 233–253.
- [13] J.K. Tien, F.S. Pettit, Mechanism of oxide adherence on Fe–25Cr–4Al (Y or Sc) alloys, *Metall. Trans.* 3 (1972) 1587–1599.
- [14] R. Cuffey, H. Buscail, E. Caudron, C. Issartel, R. Riffard, Oxidation behaviour of Kanthal A1 and Kanthal AF at 1173 K: effect of yttrium alloying addition, *Appl. Surf. Sci.* 207 (2003) 246–254.
- [15] H. Josefsson, F. Liu, J.E. Svensson, M. Halvarsson, L.G. Johansson, Oxidation of FeCrAl alloys at 500–900 °C in dry O<sub>2</sub>, *Mater. Corros.* 56 (2005) 801–805.
- [16] J.A. Nychka, D.R. Clarke, Quantification of aluminum outward diffusion during oxidation of FeCrAl alloys, *Oxid. Met.* 63 (2005) 325–352.
- [17] H. Göthlin, F. Liu, J.-E. Svensson, M. Halvarsson, L.-G. Johansson, The effect of water vapor on the initial stages of oxidation of the FeCrAl alloy Kanthal AF at 900 °C, *Oxid. Met.* 67 (2007) 251–266.
- [18] A.R. Put, K.A. Unocic, M.P. Brady, B.A. Pint, Performance of chromia- and alumina-forming Fe- and Ni-base alloys exposed to metal dusting environments: the effect of water vapour and temperature, *Corros. Sci.* 92 (2015) 58–68.
- [19] R. Fetzter, A. Weisenburger, A. Jianu, G. Müller, Oxide scale formation of modified FeCrAl coatings exposed to liquid lead, *Corros. Sci.* 55 (2012) 213–218.
- [20] E. Airiskallio, E. Nurmi, M.H. Heinonen, I.J. Väyrynen, K. Kokko, M. Ropo, M.P.J. Punkkinen, H. Pitkänen, M. Alatalo, J. Kollár, B. Johansson, L. Vitos, High temperature oxidation of Fe–Al and Fe–Cr–Al alloys: the role of Cr as a chemically active element, *Corros. Sci.* 52 (2010) 3394–3404.
- [21] M. Boualam, G. Beranger, M. Lambertin, Oxidation of an alumina-forming alloy: morphological and structural study, *Microsc. Oxid.* 2, Proc. Int. Conf., 2nd, 1993, pp. 243–252.
- [22] H. Al-Badair, G.J. Tatlock, The influence of moisture content of the atmosphere on alumina scale formation and growth during high temperature oxidation of PM2000, *Mater. High Temp.* 17 (2000) 133–137.
- [23] A. Kolb-Telieps, U. Miller, H. Al-Badair, G.J. Tatlock, D. Naumenko, W.J. Quadackers, G. Strehl, G. Borchardt, R. Newton, J.R. Nicholls, M. Maier, D. Baxter, The Role of bioxidant corrodents on the lifetime behavior of FeCrAl(RE) alloys. Lifetime Modeling of High Temperature Corrosion Processes, Proceedings of an EFC Workshop, vol. 34, 2001, pp. 123–134.
- [24] K. Onal, M.C. Maris-Sida, G.H. Meier, F.S. Pettit, Water vapour effects on the cyclic oxidation resistance of alumina forming alloys, *Mater. High Temp.* 20 (2003) 327–337.
- [25] H. Buscail, S. Heinze, Ph. Dufour, J.P. Larpin, Water–vapor-effect on the oxidation of Fe–21.5 wt.%Cr–5.6 wt.%Al at 1000 °C, *Oxid. Met.* 47 (1997) 445–465.
- [26] I. Kvernes, M. Oliveira, P. Kofstad, High temperature oxidation of Fe–13Cr–xAl alloys in air/water vapor mixtures, *Corros. Sci.* 17 (1977) 237–252.
- [27] P.T. Moseley, K.R. Hyde, B.A. Bellamy, The microstructure of the scale formed during the high temperature oxidation of a Fe–Cr alloy steel, *Corros. Sci.* 24 (1984) 547–565.
- [28] T. Liu, C. Wang, H. Shen, W. Chou, N.Y. Iwata, A. Kimura, The effects of Cr and Al concentrations on the oxidation behaviour of oxide dispersion strengthened ferritic alloys, *Corros. Sci.* 76 (2013) 310–316.



- [29] A.D. Smigellkas, E.O. Kirkendall, Zinc diffusion in alpha brass, *Trans. AIME* 171 (1947) 130–142.
- [30] C.M. Wang, D.R. Baer, L.E. Thomas, J.E. Amonette, J. Antony, Y. Qiang, G. Duscher, Void formation during early stages of passivation: initial oxidation of iron nanoparticles at room temperature, *J. Appl. Phys.* 98 (2005). 094308-094308–7.
- [31] W.J. Quadakkers, H. Holzbrecher, K.G. Briefs, H. Beske, Difference in growth mechanism of oxide scales formed on ODS and conventional wrought alloys, *Oxid. Met.* 32 (1989) 67–88.
- [32] T. Yamashita, P. Hayes, Analysis of XPS spectra of  $\text{Fe}^{2+}$  and  $\text{Fe}^{3+}$  ions in oxide materials, *Appl. Surf. Sci.* 254 (2008) 2441–2449.
- [33] C.R. Brundle, T.J. Chuang, K. Wandelt, Core and valence level photoemission studies of iron oxide surfaces and the oxidation of iron, *Surf. Sci.* 68 (1977) 459–468.
- [34] C.Q. Cheng, J. Zhao, T.S. Cao, Q.Q. Fu, M.K. Lei, D.W. Deng, Facile chromaticity approach for the inspection of passive films on austenitic stainless steel, *Corros. Sci.* 70 (2013) 235–242.
- [35] X. Liu, Y. Shao, Y. Zhang, G. Meng, T. Zhang, F. Wang, Using high-temperature mechanochemistry treatment to modify iron oxide and improve the corrosion performance of epoxy coating – I. High-temperature ball milling treatment, *Corros. Sci.* 90 (2015) 451–462.
- [36] T. Fujii, F. De Groot, G. Sawatzky, F. Voogt, T. Hibma, K. Okada, In situ XPS analysis of various iron oxide films grown by  $\text{NO}_2$ -assisted molecular-beam epitaxy, *Phys. Rev. B* 59 (1999) 3195–3202.
- [37] Y. Gao, S.A. Chambers, Heteroepitaxial growth of  $\alpha\text{-Fe}_2\text{O}_3$ ,  $\gamma\text{-Fe}_2\text{O}_3$  and  $\text{Fe}_3\text{O}_4$  thin films by oxygen-plasma-assisted molecular beam epitaxy, *J. Cryst. Growth* 174 (1997) 446–454.
- [38] P. Kofstad, *High Temperature Corrosion*, Elsevier Applied Science, London/New York, 1988, pp. 408–412.
- [39] F.H. Stott, G.C. Wood, J. Stringer, The influence of alloying elements on the development and maintenance of protective scales, *Oxid. Met.* 44 (1995) 113–145.
- [40] F. Liu, H. Götlind, J.-E. Svensson, L.-G. Johansson, M. Halvarsson, Early stages of the oxidation of a FeCrAlRE alloy (Kanthal AF) at 900 °C: a detailed microstructural investigation, *Corros. Sci.* 50 (2008) 2272–2281.
- [41] H. Hu, Z. Zhou, M. Li, L. Zhang, M. Wang, S. Li, C. Ge, Study of the corrosion behavior of a 18Cr-oxide dispersion strengthened steel in supercritical water, *Corros. Sci.* 65 (2012) 209–213.
- [42] J. Yuan, W. Wang, S. Zhu, F. Wang, Comparison between the oxidation of iron in oxygen and in steam at 650–750 °C, *Corros. Sci.* 75 (2013) 309–317.
- [43] L. Liu, Z.G. Yang, C. Zhang, M. Ueda, K. Kawamura, T. Maruyama, Effect of water vapour on the oxidation of Fe–13Cr–5Ni martensitic alloy at 973 K, *Corros. Sci.* 60 (2012) 90–97.